Graded recruitment of pupil-linked neuromodulation by parametric stimulation of the vagus nerve

Z. Mridha[1,2,*], J. W. de Gee[1,2,*], Y. Shi[1,2], R. Alkashgari[3], J. Williams[3], A. Suminski[3], M. P. Ward[4], W. Zhang[1,2], M. J. McGinley[1,2,5]

[1]Department of Neuroscience, Baylor College of Medicine, Houston, TX, USA; [2]Jan and Dan Duncan Neurological Research Institute, Texas Children's Hospital, Houston, TX, USA; [3]Department of Biomedical Engineering, , Madison, WI, USA; [4]Department of Biomedical Engineering, Purdue University, West Lafayette, IN, USA; [5]Department of Electrical and Computer Engineering, Rice University, Houston, TX, USA.

(* equal contribution)

Address correspondence to: matthew.mcginley@bcm.edu

ABSTRACT

Vagus nerve stimulation (VNS) is thought to alter the state of the brain by recruiting global neuromodulators. VNS is used in treatment-resistant epilepsy, and is increasingly being explored for other brain disorders, such as depression, and as a cognitive enhancer. However, the promise of VNS is only partially fulfilled due to a lack of mechanistic understanding of the transfer function between stimulation parameters and neuromodulatory response, together with a lack of biosensor for assaying stimulation efficacy in real time. We here develop an approach to VNS in head-fixed mice on a treadmill, and use it to show that pupil dilation is a biosensor for VNS-evoked cortical neuromodulation. In a 'goldilocks' zone of stimulation parameters, current leakage and off-target effects are minimized and the extent of pupil dilation tracks VNS-evoked basal-forebrain cholinergic axon activity in auditory cortex. Thus, pupil dilation is a sensitive readout of the moment-by-moment titratable effects of VNS on brain state.

INTRODUCTION

The vagus nerve carries efferent parasympathetic and afferent sensory information between the brain and body. Early work showed that stimulation of the vagus nerve (VNS) caused gross changes in the electro-encephalogram (Bailey and Bremer, 1938) and acutely suppresses seizure activity (Zabara, 1985). For over 30 years since then, VNS has been in wide use as an epilepsy treatment (Groves and Brown, 2005). In addition, VNS is currently explored in other brain disorders, such as major depression, anxiety, autism, tinnitus, and Alzheimer's disease (De Ridder et al., 2014; Edwards et al., 2017; Engineer et al., 2017; Fang et al., 2016; George and Aston-Jones, 2010; George et al., 2000; George et al., 2008; Nahas et al., 2005; Rush et al., 2005; Sjögren et al., 2002). Despite its wide and growing use, the mechanisms by which VNS exerts its clinical benefits are still largely unknown.

Functional neuroimaging in humans and c-fos imaging in rats show VNS-evoked activity in many brain regions, including amygdala, thalamus, hypothalamus, and cerebral cortex (Chae et al., 2003; Naritoku et al., 1995). This widespread brain activation pattern, together with the functional anatomy of the direct connections of the vagus nerve with the brain, suggest a prominent role for global neuromodulatory

systems. Indeed, lesions of the noradrenergic locus coeruleus (LC) occlude the seizure-attenuating effects of VNS (Krahl et al., 1998), and VNS induces phasic firing in LC neurons that increases in intensity with increasing VNS pulse width and amplitude (Groves et al., 2005; Hulsey et al., 2017). In addition, effects of VNS on cortical excitability synchrony are occluded by blockade of muscarinic receptors in auditory cortex, suggesting a role for acetylcholine released by the basal forebrain (Nichols et al., 2011). The occlusion in these lesion and pharmacological studies is difficult to interpret, because the bluntness of the manipulations may have unphysiological knock-on effects on the true mechanisms. Therefore, whether and which neuromodulators mediate the therapeutic benefits of VNS is unknown.

In sensory and motor systems, VNS-evoked cortical neuromodulation is increasing being explored for therapeutic benefits in a Hebbian framework, by temporally pairing VNS with sensory stimulation or movements. These studies suggest a prominent role for VNS-evoked basal forebrain acetylcholine release in neocortex. On the motor side, VNS paired with forelimb movements drives reorganization of representations in motor cortex; the plasticity is lost after lesions of cortical cholinergic projections from the basal forebrain (Hulsey et al., 2016). On the sensory side, pairing sound presentation with VNS results in auditory cortical map reorganization similar to that observed when sound is paired with nucleus basalis stimulation (Engineer et al., 2011; Kilgard and Merzenich, 1998). However, it has not been demonstrated whether VNS evokes acetylcholine release from basal forebrain into the cortex, so the role of acetylcholine in VNS-evoked cortical plasticity remains speculative.

A major impediment to parse mechanisms, optimize therapeutic strategies, or adjust stimulation in real time, is the lack of established biosensors for successful VNS. The gold-standard for assessing nerve engagement is to directly measure the compound action potential (CAP) response to VNS (Evans et al., 2004; Qing et al., 2018). However, CAP recordings: 1) are not routinely done in clinical settings, 2) are impractical in small animals, 3) are invasive, and 4) do not provide a readout of central response. As a result, VNS settings are typically adjusted to "the highest 'comfortable' setting" based on patient feedback, an approach that likely contributes to variability in efficacy and impedes principled innovation (Groves and Brown, 2005; Qing et al., 2018). Non-invasive biosensor(s), that could track the brain's response to VNS, would allow more systematic optimization of treatment in each patient, and potentially open up avenues for closed-loop, adaptive stimulation strategies that respond in real time to changes in the brain (Edwards et al., 2017; George and Aston-Jones, 2010).

We and others recently showed that dilation of the pupil at constant luminance provides a sensitive, non-invasive readout of cortical and hippocampal signatures of brain state, in mice (McGinley et al., 2015a; McGinley et al., 2015b; Reimer et al., 2014; Vinck et al., 2015). Pupil dilation tracked basal forebrain cholinergic and locus coeruleus noradrenergic axonal activity in sensory cortex, with modulator-specific temporal signatures (Reimer et al., 2016). Pupil dilation also tracks neuromodulatory brain state in humans and non-human primates (de Gee et al., 2017; Joshi et al., 2016). Here, we test the hypothesis that pupil dilation can serve as a biosensor of VNS-evoked effects on neuromodulatory brain state. Indeed, we find that VNS results in pupil dilation, the magnitude of which tracks the stimulation parameters. We further show that this VNS-evoked dilation is mediated by a network involving release of acetylcholine from basal forebrain into neocortex and interacts non-linearly with the current momentary state of the brain.
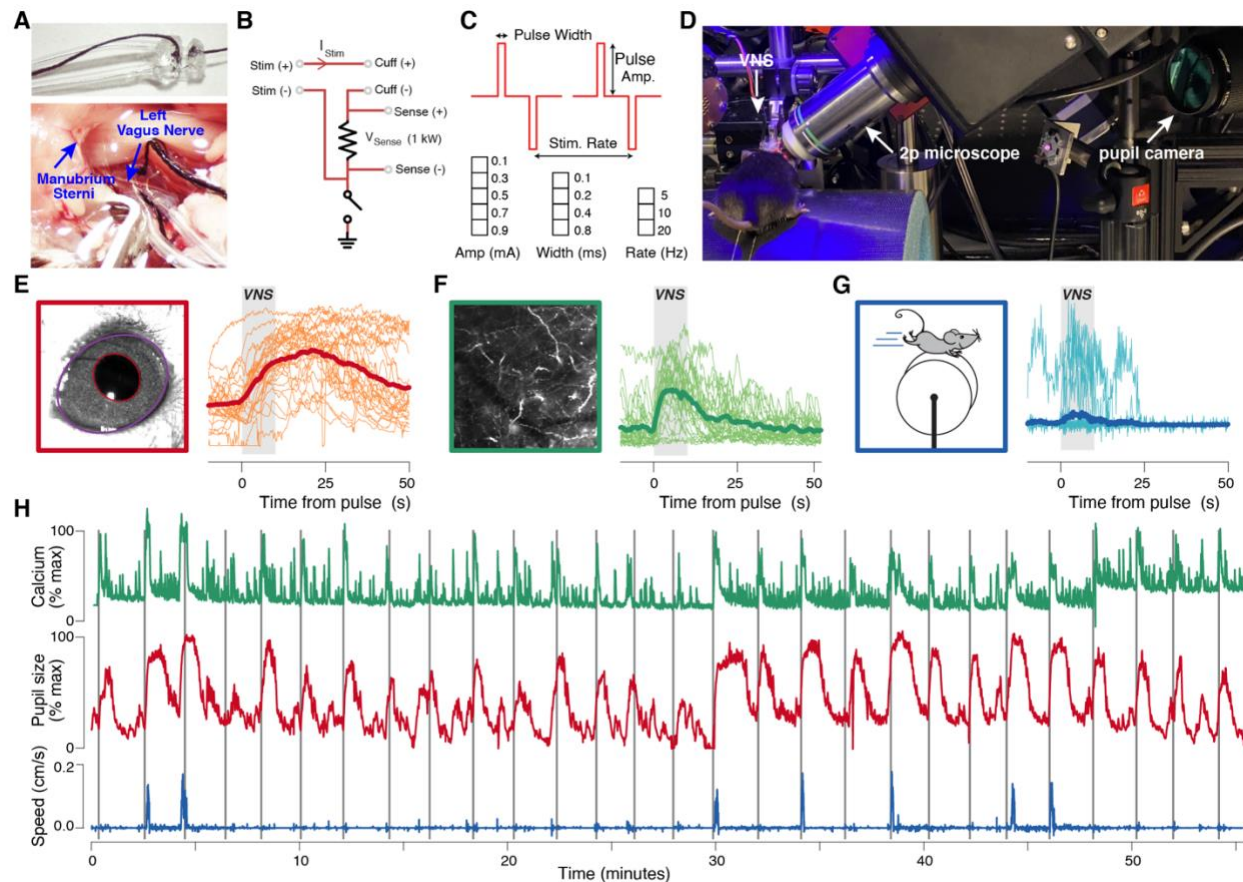
Figure 1. VNS, pupillometry, and two-photon axonal GCaMP imaging in auditory cortex of awake head-fixed mice. (A) Bipolar vagus nerve stimulator (VNS) cuff design (top) and implantation on the left cervical vagus nerve (bottom). **(B)** VNS stimulation circuit diagram. Current is applied between the two cuff electrodes using a improved Howland current pump, and return current is measured across a 1 kOhm sensing resistor. In most experiments, the animal and current pump circuit were isolated from ground (indicated at bottom). **(C)** VNS pulse waveforms and parameters. Bi-phasic pulses, separated by a gap of 50% inter-pulse interval were delivered in trains lasting 10 seconds (top). Five pulse amplitudes, four pulse widths, and three pulse rates were combined to yield 60 unique VNS parameter combinations (bottom). **(D)** Photograph of a mouse undergoing pupillometry and VNS in the two-photon imaging setup. **(E)** Left: example video frame of the mouse's eye, with fitted ellipses overlaid on the pupil (red) and exposed eye area (purple). Right: 60 pupil size time-series during an example session time-locked to each VNS train (thick line, session mean; thin lines, individual trains). Grey rectangles indicate 10 second window for each train of VNS pulses. **(F)** Left: Example mean fluorescence intensity image from *in vivo* two-photon GCaMP6 imaging of cholinergic axons in auditory cortex. Right: example axonal signal time-series, aligned as in panel E. Same session as in panel E. **(G)** Walking speed from time-series from the same session as in panels E and F. **(H)** Full session time-series of pupil size (red), fluorescence (green) and walking speed (blue) from the same session as in E-G. Narrow vertical grey rectangles indicate the time of each VNS train.

RESULTS

In order to determine if vagus nerve stimulation (VNS) results in release of acetylcholine in cortex, and if this VNS-evoked neuromodulation can be tracked using pupillometry, we developed a VNS approach in head-fixed mice. We designed and made custom cuffs for bi-polar stimulation of the vagus nerve in awake mice, based on our previous design in rats (Fig. 1A, top) (Ward et al., 2014). The cuffs were implanted on the left cervical vagus nerve (Fig. 1A, bottom). We stimulated with constant current and

measured the return current using a sensing resistor (Fig. 1B). We observed that a large fraction of applied current did not return to the negative lead of the cuff (and thus presumably leaked to ground) if the animal was grounded via the head-post (Fig. S1A). Therefore, the animal and current stimulation circuit were isolated from ground in most experiments (Fig. 1B, bottom). We stimulated with trains of bi-phasic pulses (to avoid charge accumulation) lasting 10 seconds, once every 100-140 seconds (Fig. 1C, top; Materials and Methods). For each train, the pulse amplitude, width, and repetition rate were selected from a set of 60 unique parameter combinations (Fig. 1C, bottom).

Mice were head-fixed on a cylindrical treadmill and their pupil size recorded with a custom system (Materials and Methods), and in some experiments they were underneath a two-photon microscope to image cholinergic axon activity in auditory cortex (Fig. 1D). We observed that VNS trains elicited pupil dilation (Fig. 1E), cholinergic axon activity (Fig. 1F), and walking on the treadmill (Fig. 1G), which was superimposed on spontaneous changes in these signals across each session (Fig. 1H). We found that narrow pulse widths (0.1 ms) exhibited modest amplitude reduction, and that a small amount of amplitude reduction also occurred across all parameter combinations for higher-impedance cuffs, particularly for large amplitude pulses, resulting from some combination of minor waveform distortion and current pump saturation (Fig. S1B-E). These small distortions did not affect the overall results (see below), but point to the benefits of avoiding impedances >15 kOhm and pulse widths < 0.2ms.

Graded dependence of pupil dilation on VNS parameters

To understand the parameter dependence of the VNS-evoked pupil dilation, we first plotted time-courses of VNS train-locked pupil response for each value of each parameter, while average across all values of the other two parameters. Pupil dilation had similar time-courses across parameters combinations, and the magnitude of dilation increased with increasing amplitude (Fig. 2A, left), pulse width (Fig. 2A, middle), or stimulation train rate (Fig. 2A, right). We then extracted VNS-evoked pupil response scalars in a window centered on the peak dilation (red bars at bottom in Fig. 2A). A 3D circle plot of the scalar values showed that the dilation appeared to increase from zero and then saturate, for each parameter, and that there were no apparent complex (e.g. non-multiplicative) interactions between parameters (Fig. 2B). Therefore, we fit log-logistic growth curves (Materials and Methods, eq. 3) to the scalar dilations as a function of pulse amplitude, width, and rate (Fig. 2C). The multivariate log-logistic function fit well to the observed marginal distribution patterns. The eye lid receives the same sympathetic innervation as the pupil dilator, but no parasympathetic input. Therefore, we measured the area of exposed eye. It exhibited a similar pattern to pupil dilation, suggesting a major sympathetic contribution to the VNS-evoked pupil response (Fig. S2).
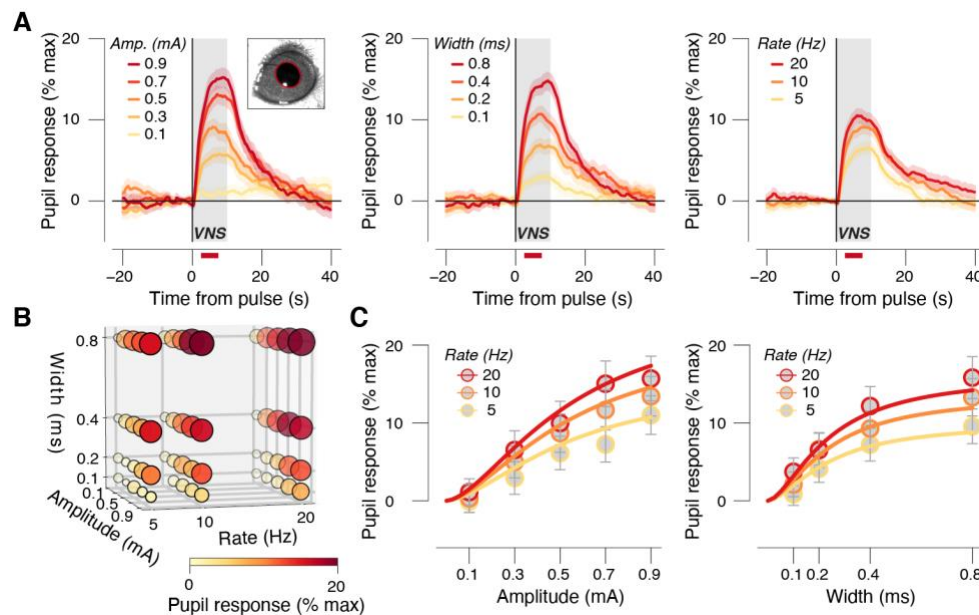
4

Figure 2. Pupil dilation has a graded dependence on VNS parameters (A) VNS-evoked pupil response time-courses separately for each pulse amplitude (left), width (middle) and rate (right), collapsed across two other stimulation parameters. Grey window, 10 second VNS train; red bars, interval for VNS-evoked pupil response scalar measures (see Materials and Methods); shading, s.e.m. **(B)** VNS-evoked pupil response measure for all 60 unique parameter combinations. Response magnitude is indicated by circle size and color. **(C)** VNS-evoked pupil response scalars plotted separately for pulse amplitudes and rates (binned across width, left) and separately for pulse widths and rates (binned across amplitude, right). Colored lines, fitted log-logistic functions (Materials and Methods); error bars, s.e.m. × 1.96 (95% confidence interval of the mean).

The visually apparent multiplicative interaction between parameter dependencies suggests that it may be possible to collapse pulse amplitude and width into a single metric: charge/pulse. Indeed, when pupil response was plotted separately for each train rate, as a function of charge/pulse, curves for different pulse widths liked approximately on top of each other (Fig. 3A and S3A). Consistent with this visual inspection, a comparable amount of variance was explained when fitting a full hyper-surface that depended on amplitude, width, and train rate (16.6%; Materials and Methods, eq. 3) versus a reduced surface that only depended on charge/pulse and train rate (16.5%; Materials and Methods, eq. 4). A similar dependence on charge/pulse has been observed for VNS-evoked LC firing rates (Hulsey et al., 2017). Therefore, to further reduce the parameter space for subsequent analyses, we defined 5 charge/pulse 'bins' that parse the range tested values into approximately equal-sized log-spaced charge bins (Fig. 3B). Using these charge, we plotted time courses (Fig. 3C) and scalars sorted by charge bin (Fig. 3D), and assessed the statistical significance of pupil dilation in each charge bin (Fig. 3D, bottom). Dilation was not significant for the smallest charge bin (Fig. 3D, blue band), but was significant for all charge bins above that (Fig. 3D, green and orange bands).

Because of the small size of the mouse neck, and the presence of other nearby nerves, we were concerned that VNS-evoked pupil dilation resulted from spread of current to other nerves, rather than from activation of the vagus nerve. Therefore, we conducted similar experiments, but severed and retracted the vagus nerve above and below the cuff. In this double-cut nerve condition, VNS no longer caused significant pupil dilation, for all but the largest charge/pulse bin (Fig. 3E,F). We therefore define the largest charge

bin as 'off target', and the intermediate charge bins as 'goldilocks' (see Figs. 3D,F). Similar results were observed if the nerve was cut only above the cuff (proximal to the brain, called single cut; Fig. S3B and C), suggesting that VNS-drive pupil dilation with intact nerve resulted from activation of afferent fibers. If, however, the animal was grounded through the head-post, we found that substantial pupil dilation occurred, even with double cut nerve (Fig. 3G,H). Substantial dilation in grounded conditions occurred during VNS with intact or single cut nerve (Fig. S3D-G), as well as substantial additional dilation after VNS train termination, which was not observed in ungrounded conditions. Thus, if care is taken to prevent current spread to ground, and charge/pulse is kept below 0.3 µC, pupil dilation provides a sensitive readout of the strength of pupil-indexed brain activation resulting selectively from vagus nerve fiber firing.
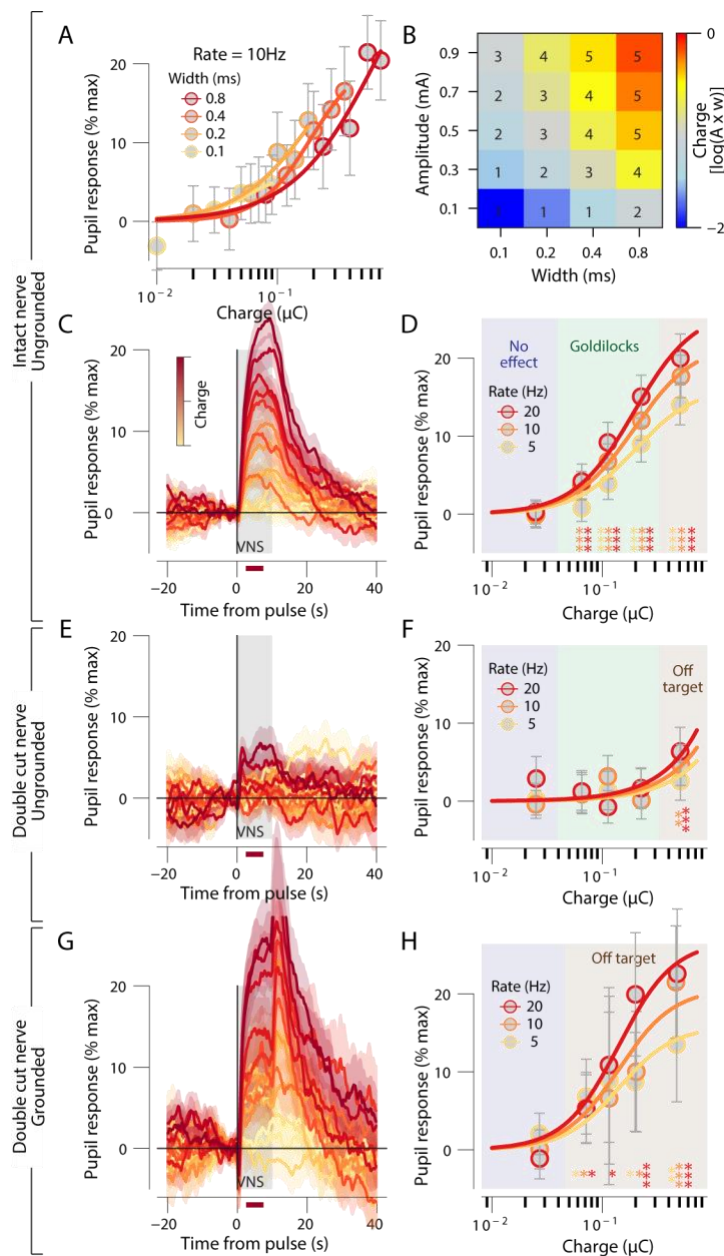

Figure 3. VNS-evoked pupil dilation requires an intact nerve and localized current. (A) VNS-evoked pupil response measures separately per pulse charge (amplitude × width) and width for 10 Hz trains. Colored lines, fitted log logistic function (see Materials and Methods); error bars, s.e.m. × 1.96 (95% confidence interval of the mean). **(B)** Grid showing the width and amplitude parameter combinations that were collapsed into our 5 charge/pulse bins. **(C)** VNS-evoked pupil time-courses, each trace is a charge/pulse bin and train rate. Grey window, VNS train; red bar, interval for VNS-evoked pupil response scalar measures (see Materials and Methods); shading, s.e.m. **(D)** VNS-evoked pupil response measures separately per charge/pulse bin and train rate. Colored lines, fitted log logistic function (see Materials and Methods); stats, one sample t-test (tested against 0; ***p < 0.001, **p < 0.01; *p < 0.05, corrected for false discovery rate); error bars, s.e.m. × 1.96 (95% confidence interval of the mean). **(E-F)** As C-D, but for double cut nerve ungrounded sessions. **(G-H)** As C-D, but for the sessions with double cut nerve and head-post grounded.

State-dependence of VNS-evoked pupil dilation

Because there are large, ongoing fluctuations in pupil size, which reflect changes in brain state (see Fig. 1H) (McGinley et al., 2015b), we wondered if the magnitude of the VNS-evoked pupil dilation depended on pre-stimulation pupil-indexed state. To test this, we conducted a series of experiments in which a single VNS parameter combination was used in all 60 repetitions of stimulation. This allowed us to post-hoc sort the responses into bins based on pre-stimulation pupil size. But because pupil size can change quickly even without stimulation, we first characterized the spontaneous tendency of the pupil to change size on the time scale of VNS-evoked pupil dilation, as a function of the baseline pupil size. To do this, we collected the pupil time-series from each 30 second window before VNS and sorted into 8 groups based on the mean pupil size in a pseudo-baseline window. Plotting the average pupil time-series in each of these 8 bins revealed a strong tendency for the pupil size to revert to the mean on the time scale of tens of seconds (Fig. 4A, left). This same mean reversion was apparent in baseline-sorted VNS-locked pupil responses (Fig. 4A, middle).

A subtraction of pseudo- from VNS-locked pupil time series successfully isolated the phasic VNS-evoked dilation from mean-reversion (Fig. 4A, right). To quantify this mean-reversion corrected baseline dependence, we calculated a correction function from a fit of a cubic function to the spontaneous (pseudo-VNS) tendency to mean-revert in the same time windows used to measure VNS-evoked pupil dilation (Fig. 4B; see black bars at bottom of Fig. 4A; see also Fig. S4A). Correcting VNS-evoked pupil response scalars with this mean-reversion function revealed an inverted-U dependence of VNS-evoked pupil response on baseline pupil size (Fig. 4C).
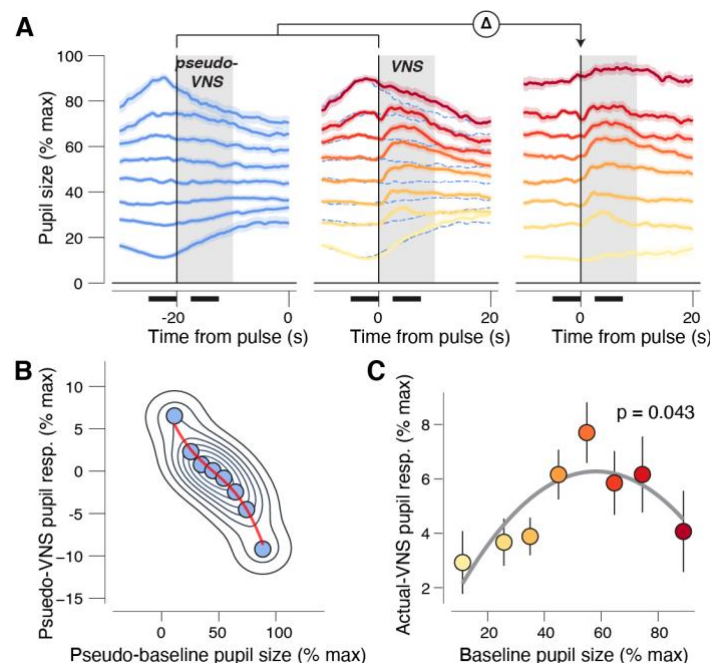

Figure 4: VNS-evoked pupil dilation has an inverted-U dependence on baseline arousal state. (A) Left: Pupil size time-courses in the 30 seconds before each VNS stimulus train, sorted into eight bins of pseudo-baseline pupil size (mean pupil size from -25 to -20 seconds before each VNS). These sorted traces illustrate that spontaneous pupil fluctuations exhibit a strong tendency to revert to the mean. Middle: same as at left, but for pupil size time-course from 10 seconds before to 20 seconds after VNS. Blue dashed lines reproduce the spontaneous fluctuations shown at

left. Note the VNS-evoked responses ride on top of the general tendency of reversion to the mean. Right: difference (subtraction) of the middle and left panels, shifted to their appropriate baselines. Note the several seconds-long VNS-evoked dilation seen from mid-size baseline, but not large or small baseline. **(B)** Relationship between pseudo-VNS pupil responses and pseudo baseline pupil size (panel A, left). Red line, fitted cubic function (Materials and Methods). **(C)** Relationship between VNS-evoked pupil responses, after correction for reversion to the mean (Materials and Methods) as a function of pre-VNS baseline pupil size. Grey line, fitted $2nd$ order polynomial (Materials and Methods); stats, sequential polynomial regression (Materials and Methods); error bars, s.e.m.

VNS activates cholinergic axons in auditory cortex

Having now demonstrated that VNS results in dilation of the pupil, we wondered which neuromodulator system(s) were activated in association with the VNS-evoked pupil dilation. We previously showed that long-lasting (e.g. >2-3 seconds) pupil dilation closely tracks cholinergic axonal activity in auditory and visual cortex in similar behavioral conditions to those used in this study (Reimer et al., 2016). Therefore, we suspected that VNS-evoked pupil dilation was linked to release of acetylcholine from basal forebrain into the cortex (BF-ACh). To test this hypothesis, we imaged populations of BF-ACh axons in auditory cortex in mice conditionally expressing GCaMP6s in cholinergic neurons (Materials and Methods). We observed an often dense plexus of axons in layer I of auditory cortex, consistent with the known anatomical innervation pattern (Fig. 5A, left). To ask how activity in these axons was linked to VNS stimulation, we first calculated the cluster-corrected pixel-wise significance of the BF-ACh axon response to VNS (irrespective of VNS parameters). This approach provides an unbiased search for significant pixels, similar to what is commonly done with fMRI imaging. We found that the significant pixels mapped closely to a large majority of the plexus of axons (Fig. 5A, right), and that this activity was not a result of brain motion (Fig. S5A-C).

To explore the parameter dependence of VNS-evoked BF-ACh axon activity, we tested all combinations of a reduced parameter set compared to that used with the full exploration of pupil dilation (see Fig. S5G). This was done in order to keep the imaging sessions within 1 hour and avoid excessive bleaching and/or photo-damage to the tissue. We found that the VNS-evoked BF-ACh axon activity exhibited a similar parameter dependence (Fig. 5B,D) and time-course (Fig. 5C) to that of pupil dilation seen above (and see Fig S5D-H). Indeed, significant axonal activity was observed in the same goldilocks zone of parameter space, and saturated before entering the off-target zone (Fig. 5E; to avoid 'double dipping', we tested for significant by comparing the VNS-evoked calcium responses in the highest four charge bins to responses in the lowest charge bin, Materials and Methods). Thus, parametrically varied VNS results in titratable release of acetylcholine in cortex.
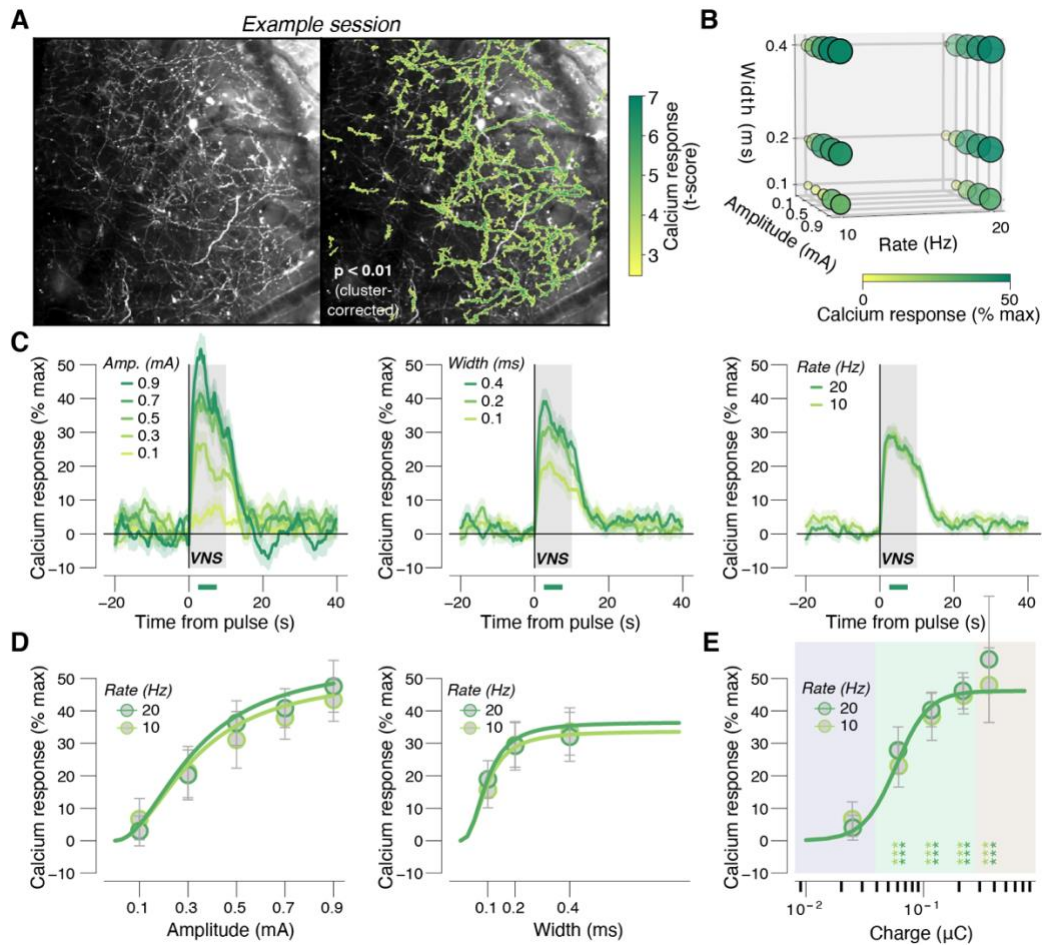
8

Figure 5: VNS causes graded neuromodulation recruitment. (**A**) Left: example session mean fluorescence of cholinergic axons in layer 1 of auditory cortex. Right: as left, but with overlaid color map of VNS-evoked calcium response measure t-score (across all VNS stimulations; see Materials and Methods). This map was used as a session-wise region of interest for analysis of calcium signal parameter dependence (**B**) VNS-evoked calcium response measures (Materials and Methods) for all 30 unique parameter combinations. Response magnitude is indicated by circle size and color. (**C**) VNS-evoked calcium responses separately for pulse amplitudes (left), widths (middle) and rates (right) collapsed across two other stimulation parameters. Grey window, 10 second VNS train; green bar at bottom, interval for VNS-evoked axonal calcium response measures (Materials and Methods); shading, s.e.m. (**D**) VNS-evoked calcium response measures separately for pulse amplitudes and rates (left, collapsed across width) and separately for pulse widths and rates (right, collapsed across amplitudes). Colored lines, fitted log logistic function (Materials and Methods); error bars, s.e.m. $\times 1.96$ (95% confidence interval of the mean). (**E**) Same as in D, but for charge/pulse bins. Stats, paired-samples t-test (tested against the response magnitudes in the lowest charge bin; ***p < 0.001, **p < 0.01; *p < 0.05 false discovery rate corrected).

VNS effects on pupil-indexed neuromodulation do not depend on locomotion

In addition to causing pupil dilation, we observed that animals sometimes walked on the treadmill during and shortly after trains of VNS. We therefore analyzed the probably of walking as a function of the VNS parameters. We defined walking very liberally, as an average velocity during VNS of greater than 0.05 cm/second (Fig. S6). Even with this liberal criterion, walking occurred on a substantial fraction of trials only for fairly strong stimulation, and maxed out at about 40% probability in the off-target stimulation zone (Fig. 6A, B). To further characterize the VNS-evoked walking, we measured the distance traveled time-

9

courses for those trials with significant walking. When mice walked, they did so mostly during the stimulation, and stopped shortly afterwards, and the distance traveled appeared weakly parameter dependent (Fig. 6C,D). To quantify the parameter dependence, we calculated the mean speed during the 10 seconds of VNS for those trains that elicited significant dilation. Average walking speed during the 10 second trains, for those trains with significant walking, depended weakly on pulse amplitude (Fig. 6E, left) and even less so on pulse width (Fig. 6E, right) or stim rate (Fig. 6E, both panels, and 6F). Thus, when walking did occur, it manifested as a fairly stereotyped walk-bout at 0.3-0.4 cm/second lasting the duration of the VNS, followed by slowing to a stop.
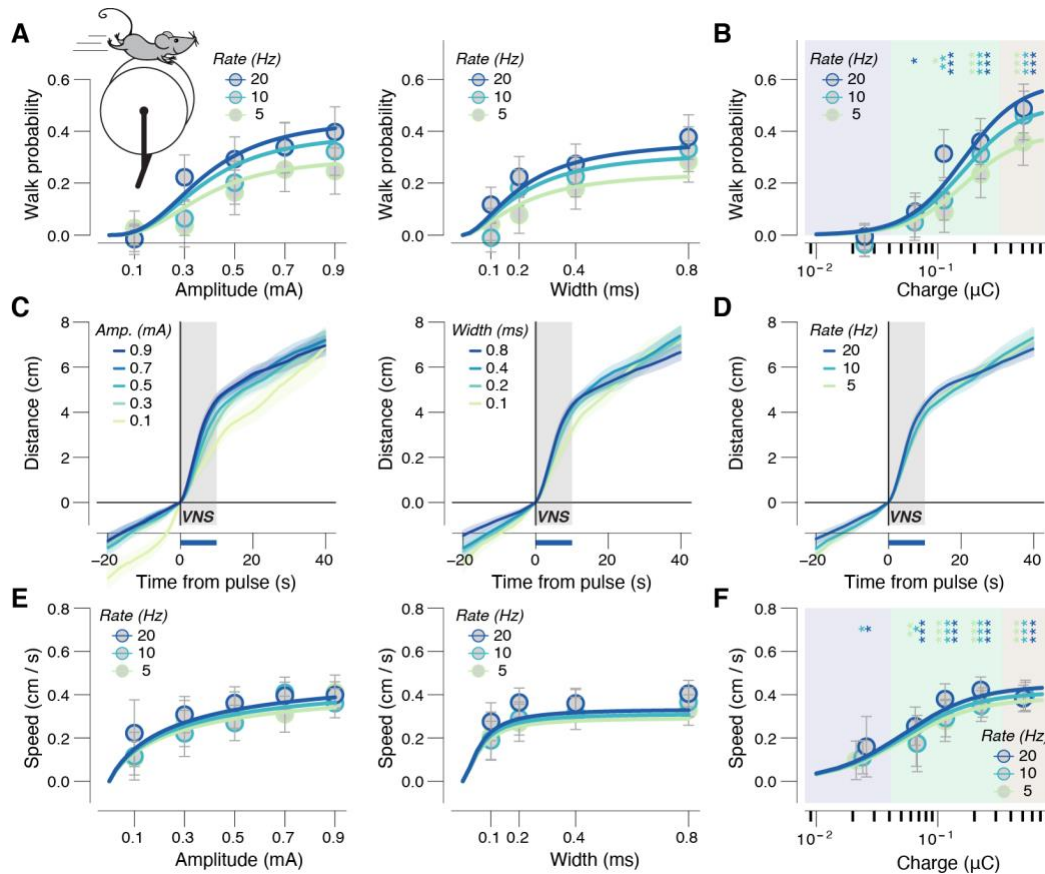

Figure 6: VNS causes graded locomotor activity. (A) VNS-evoked walk probability (see Materials and Methods) separately for pulse amplitudes and rates (left) and separately for pulse widths and rates (right). Colored lines, fitted log logistic function (Materials and Methods); error bars, s.e.m. $\times$ 1.96 (95% confidence interval of the mean). **(B)** Same as in A, but for charge bins. Stats, one sample t-test (tested against 0; ***$p < 0.001$, **$p < 0.01$; *$p < 0.05$ false discovery rate corrected). **(C)** Walked distance (walk trials only) after VNS train start, separately for pulse amplitudes (left), widths (middle) and rates (right) collapsed across two other stimulation parameters. Red window, pulse duration; black bar, interval for VNS-evoked velocity measures (Materials and Methods); shading, s.e.m. **(E-F)** Same layout as in A-B, but for walking velocity on walk trials only.

In our BF-ACh imaging experiments, we had measurements of VNS stimulus parameters and VNS-evoked axonal activity, pupil dilation, and walking patterns. We sought to understand the interdependence of these four variables. First, we excluded VNS trains with walking and plotted the calcium response and

10

pupil dilation as a function of charge/pulse (Fig. S7A). We found that axonal response (Fig. 7A) and pupil dilation (Fig. 7B) exhibited a similar parameter dependence to that observed previously (without excluding walking trials). Therefore, we concluded that VNS-evoked pupil-indexed neuromodulation did not depend on locomotor activity. Having removed walking from the picture, we then compared the VNS train-wise magnitudes of pupil response and calcium response. We found VNS-evoked pupil dilation and BF-ACh axonal activity were highly correlated (Fig. 7C).

To further characterize the effects of VNS on ACh release and pupil dilation, we conducted a mediation analysis, asking to what extent VNS-evoked ACh statistically mediates the apparent effect of VNS on pupil dilation (Fig. 7D and Fig. S7B). We found that the indirect path of VNS driving ACh, in turn driving pupil dilation, statistically mediates most of the apparent effect of VNS on pupil, with no significant direct effect of VNS on pupil (Fig. 7E). Similar results of the mediation analysis are observed if walking trials are included, although the direct path now has a significant component as well (Fig. S7C,D). Taken together, we conclude that pupil dilation provides a sensitive readout of VNS-evoked cholinergic modulation of cortex.
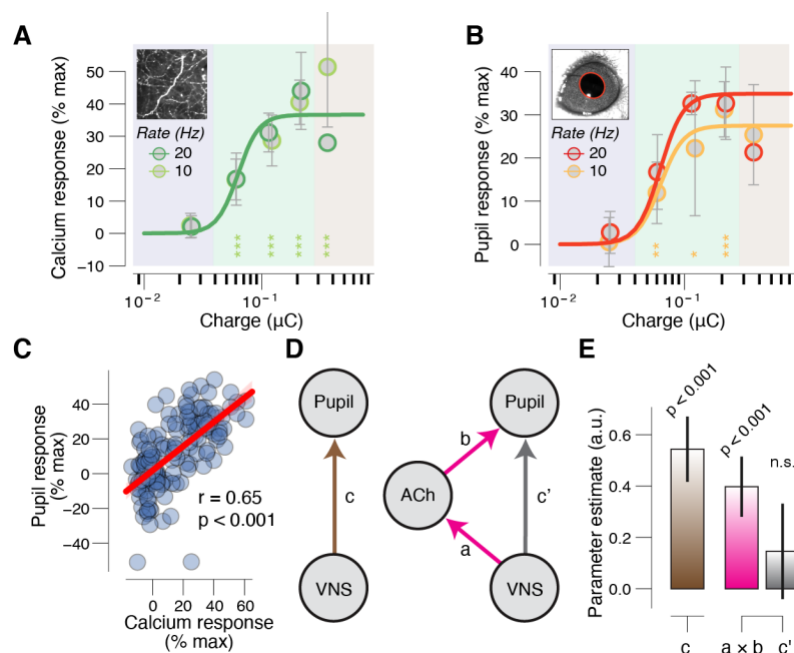

Figure 7: VNS triggered cortical acetylcholine release mediates a large fraction of pupil dilation. (A) VNS-evoked calcium response measures, in absence of walking, separately per charge/pulse bin and train rate. Colored lines, fitted log logistic function (Materials and Methods); stats, one sample t-test (tested against 0; ***$p < 0.001$, **$p < 0.01$; *$p < 0.05$ false discovery rate corrected); error bars, s.e.m. $\times$ 1.96 (95% confidence interval of the mean). **(B)** Same as in A, but for VNS-evoked pupil responses during the imaging sessions. **(C)** Scatterplot of the relationship between VNS-evoked pupil responses and VNS-evoked calcium responses, in absence of walking. Data points are individual VNS trains; red line, linear fit, stats, Pearson correlation. **(D)** Left, schematic of relationship between VNS and pupil responses. Arrow, regressions; coefficient *c* quantifies the 'total effect'. Right, schematic of mediation analysis of VNS to pupil responses, via cholinergic axons responses (Materials and Methods). Arrows, regressions; coefficient *a* $\times$ *b* quantifies the 'indirect' (mediation) effect; coefficient *c'* quantifies the 'direct effect'. **(E)** Fitted regression coefficients of the total effect (brown), indirect path (mediation; pink) and the direct path (grey). Error bars, 95% confidence interval (bootstrapped; 5K replicates); stats, fraction of bootstrapped coefficients smaller than 0.

DISCUSSION

Vagus nerve stimulation (VNS) is a widely used clinical therapy that is thought to exert its benefits by changing the neuromodulatory state of the brain. However, it has not been clear which neuromodulators are evoked by VNS. Furthermore, because there has not been an established biosensor to titrate stimulation on a patient-by-patient basis, or in real time, adjustments are made only coarsely, based on patient feedback. Here, we have demonstrated that pupil dilation is a sensitive readout of VNS strength and of the extent of evoked release of acetylcholine in sensory cortex. Furthermore, using single and double cut nerve experiments, together with careful measurement of impedance and current leakage, we have defined the space of optimal stimulus parameters and grounding conditions. Our approach can be applied to use VNS to achieve titratable cortical neuromodulation in closed-loop frameworks with pupil dilation as a feedback signal.

A major impediment to parsing mechanisms, optimizing therapeutic strategies, or adjusting stimulation in real time, is the lack of established biosensors for successful VNS. Our paper establishes pupil dilation as a reliable biosensor of efficacious VNS (nerve engagement without off target effects). This could be especially useful during 'transcutaneous' VNS (t-VNS) (Ellrich, 2011), to achieve fully non-invasive closed-loop VNS applications. Transcutaneous VNS is a recent development that holds promise for non-invasive and low-risk stimulation of the vagus nerve, by electrically stimulating its cervical or auricular branches, which are situated close to the surface of the skin of the neck and outer ear, respectively. However, it was recently reported that t-VNS though its auricular branch did not affect pupil size (Keute et al., 2019; Warren et al., 2019). The discrepancy between these findings and ours implies that the transcutaneous protocol likely insufficiently stimulated the vagus nerve, perhaps due to the site of stimulation (auricular vs cervical branches) or due to the chosen stimulation parameters (pulse amplitude, width, rate). Supporting this interpretation, the Keute et al. study also failed to observe behavioral effects of t-VNS, suggesting a failure to sufficiently engage the nerve.

Acetylcholine is heavily involved in normal executive and mnemonic functioning, and the loss of cholinergic signaling and cognitive decline are closely linked (Ballinger et al., 2016; Dayan, 2012; Parikh et al., 2007). Our results open up the possibility that the (therapeutic) benefits of VNS are partly mediated by the recruitment of the basal forebrain acetylcholine system. Exploring this hypothesis in the mouse model might prove to be particularly fruitful, given the genetic tools for dissecting and perturbing neural circuits at the micro- and meso-levels and the various disease models available, such as of Alzheimer's disease (Götz et al., 2018; Groves and Brown, 2005; Sjögren et al., 2002).

Our results are important for the mechanistic interpretation of pupil size measurements, a technique whose use is growing exponentially (Kret and Sjak-Shie, 2019). Pupil response is commonly used as a non-invasive peripheral readout of changes in cortical neuromodulatory arousal state (Larsen and Waters, 2018; McGinley et al., 2015b; Reimer et al., 2016). Changes in pupil diameter are also associated with locus coeruleus (LC) responses in humans (de Gee et al., 2017; Murphy et al., 2014), monkeys (Joshi et al., 2016; Varazzani et al., 2015), and mice (Breton-Provencher and Sur, 2019; Reimer et al., 2016). Our results add to a growing appreciation that pupil responses track not only activity of the LC, but also that of other subcortical regions, including the dopaminergic midbrain, the tectum, and indeed the cholinergic basal forebrain (Colizoli et al., 2018; de Gee et al., 2017; Joshi et al., 2016; Reimer et al., 2016).

The finding that VNS-evoked pupil responses and baseline pupil size interact in a non-monotonic (inverted U) fashion suggests that the largest VNS-evoked responses of cholinergic axons likewise occurred

12

for intermediate levels of tonic arousal. This result supports the model that phasic neuromodulatory signals that occur naturally are strongest during intermediate levels of tonic neuromodulatory activity (Aston-Jones and Cohen, 2005). This model is further supported by recent observations that tonic arousal predicts non-monotonic (inverted U) changes in the signal-to-noise ratio of sensory cortical responses and perceptual sensitivity (McGinley et al., 2015a; Schriver et al., 2018; Waschke et al., 2019). Note that we observed the inverted U relationship after correcting for a general reversion to mean. Reversion to the mean predicts the commonly observed linear anti-correlation between baseline pupil size and task-evoked responses (de Gee et al., 2014; Gilzenrat et al., 2010). We believe this mean reversion is under-appreciated in the analysis of pupil responses and may merit reinterpretation of a large literature on pupil dependencies of physiology and behavior.

We also observed walking in response to VNS in some cases, particularly with high shock strengths. However, we believe pupil dilation is the more useful biomarker for a number of reasons. First, our finding that VNS-evoked pupil responses occur even in the absence of walking suggests that pupil dilation is the more sensitive read-out. Second, walking occurred only probabilistically, and at higher shock strengths. Third, humans experience voluntary control over walking, while pupil dilation is largely involuntary. Fourth, pupil size measurements require nothing more than constant luminance levels and a relatively still head, so there are less restrictions on the experimental setup. In contrast, measuring walking requires a treadmill, which is particularly problematic in combination with human functional neuroimaging.

As VNS is increasingly applied to a broad range of brain disorders, validation of biosensors, elucidation of mechanisms, and optimization of stimulation techniques will be integral components of achieving success. Our results demonstrate that pupil dilation can be used as biosensor, that cortical release of acetylcholine is a component mechanism, and that control of impedance, current leakage, and stimulus parameters provide important ingredients for the improved use of VNS.

<div align="center">MATERIALS AND METHODS</div>

Animals

All surgical and animal handling procedures were carried out in accordance with the ethical guidelines of the National Institutes of Health and were approved by the Institutional Animal Care and Use Committee (IACUC) of Baylor College of Medicine. We used a cross of two transgenic lines for the imaging experiments, and wild-type mice in all other experiments. The mice for cholinergic axon imaging (n=8; 2 female; age, 8–18 weeks) were heterozygous for the ChAT-cre (Jackson labs strain B6; 129S6-Chattm1(cre)Lowl/J) and Ai162 GCaMP6 reporter lines (Allen Institute). The wild-type mice (n=30; all male) were also of C57BL/6 strain (Jackson Labs). Mice had food and water ad libitum and were individually housed after VNS cuff implantation. Mice were kept on a regular light-dark cycle, and all experimental manipulations were done during the light phase.

Vagus nerve stimulator cuff design

We adapted the implanted cuff design from prior work in rats(Ward et al., 2014). The bipolar stimulating cuff was custom built based around an improved Howland Current Pump (Texas Instruments) driven by an 18-bit NI DAQ (National Instruments). Two platinum-iridium wires were fixed 1 mm apart to biocompatible micro silicone tube (cuff: 0.5 mm inner diameter, 1.0 mm outer diameter, 2.0 mm long; lead: 0.3 mm inner diameter, 0.6 mm outer diameter, 30 mm long). The end of the two lead wires were connected to gold pins (363A/PKG, Plastic One), which were used to connect the cuff to the stimulator.

Surgical procedures

The surgical station and instruments were sterilized prior to each surgical procedure. Isoflurane anesthetic gas (2–3% in oxygen) was used for the entire duration of all surgeries. The temperature of the mouse was maintained between 36.5°C and 37.5°C using a homoeothermic blanket system.

Head post implantation. After anesthetic induction, the mouse was placed in the stereotaxic. The surgical site was shaved and cleaned with scrubs of betadine and alcohol. A 1.5-2 cm incision was made along the scalp mid-line, the scalp and overlying fascia are retracted from the skull. A sterile head post was then implanted using dental cement.

Cervical vagus nerve cuff electrode implantation. Following induction, the mouse was placed in a supine position; the surgical site was shaved and cleaned with scrubs of betadine and alcohol. A 1-1.5 cm long midline incision was made from manubrium to jaw line. Blunt dissection technique was used for the whole procedure. With tiny blunt-tipped scissors the left submaxillary gland was separated from the connective tissue and retracted to other side. The connective tissue between the left sternocleidomastoid and the sternohyoid /omohyoid was carefully separated until the carotid sheath was visible. Using a small pair of surgical retractors to hold the muscles apart, a 4-5 mm segment of the left cervical vagus nerve was dissected from the carotid sheath and the cuff electrode was positioned around the vagus nerve. We ensured that the electrode wires had circumferential or near-circumferential contact with the nerve. The cuff was fastened with silk suture. The muscles were placed back in their original position and absorbable suture was used to secure the cuff in position. A subcutaneous tunnel was made in between ear and eyes from neck incision to the top of the head, which allowed passing the cuff leads to the skull. Lead pins were fixed to the pre-exciting head post using acrylic dental cements. The submaxillary gland was placed back to its original position and the incision was sutured. While still under anesthesia, VNS response was recorded

using a pulse-oximeter (Starr Life Sciencvs, MouseOx Plus), a reductions in blood oxygen saturation was observed when stimulation was given through the implanted cuff, confirming that the electrode was appropriately positioned to stimulate the intact and functioning vagus nerve.

Craniotomy. A cranial window over the right auditory cortex was made as previously described(McGinley et al., 2015a; Reimer et al., 2016). In brief, a 3 mm window was opened using a handheld dental drill (Osada Exl-M-40). The exposed dura was then covered with a thin layer of silicon oil and a coverslip was applied over the window and sealed with surgical glue (Vetbond, 3M).

Vagus nerve stimulation protocol

Custom LabView software handled data acquisition and synchronization with vagus nerve stimulations. The vagus nerve stimulation leads were connected to the output of an enhanced Howland Current Pump (HCP) with a current scaling factor of 1 mA/V. A data acquisition board (National Instruments USB-6353 X Series) was used to interface with a computer running MATLAB R2016. Vagus nerve stimulation via our cuff was well-tolerated by our mice for up to several months. Cuff impedance was monitored frequently (before most sessions) using an Electrode impedance tester (BAK Electronics, INC: IMP-2).

Animals were allowed to recover for 2–3 days prior to recordings. The animal's head was fixed, and they were allowed to spontaneously walk or stand still on a cylindrical treadmill along a single axis of rotation. In all experiment, VNS pulses occurred at 100-140 second intervals (varied to reduce expectancy), and each pulse train lasted for 10 seconds. We performed four different types of experiments: First, in the 'parameter exploration' experiment (Figs. 2, 3, 6), we performed an exhaustive search across a three-dimensional VNS parameter space: five pulse amplitudes (0.1, 0.3, 0.5, 0.7 or 0.9 mA), four pulse widths (0.1, 0.2, 0.4 or 0.8 ms) and three pulse rates (5, 10 or 20 Hz). Each unique parameter combination (60 in total) occurred once in a session of two hours. Second, in the 'baseline pupil dependence' experiment, we administered 60 pulses with the same combination of parameter in each session: amplitude, 0.5 or 0.7 mA; width, 0.2 ms; rate, 10 or 20 Hz rate. Third, in the 'axon imaging experiment' (Figs. 5 & 7), we performed an exhaustive search across a subset of the three-dimensional VNS parameter space: five pulse amplitudes (0.1, 0.3, 0.5, 0.7 or 0.9 mA), three pulse widths (0.1, 0.2, or 0.4 ms) and two pulse rates (10 or 20 Hz). Each unique parameter combination (30 in total) occurred once in a session of one hour. Fourth, the 'light control experiment' (Fig. S5H), was the same as the axon imaging experiment, except for that we increased the background luminance in the imaging setup to our standard level in the non-imaging setups.

Grounded vs ungrounded sessions. In most experiments, to unground the animals, we put insulating tape between head-post holder and other metal parts connected to it. In grounded animal experiments, a wire connected the head-post holder to ground. To assay the effects of grounding on cuff performance, the applied current was compared to the measured return current by measuring the return current across a current-sensing resistor.

Acquisition of pupil, exposed eye area, and walking data

We continuously recorded the eye contralateral to the cuff implantation with a Basler GigE camera (acA780-75gm), coupled with a fixed focal length lens (55 mm EFL, f/2.8, for 2/3"; Computar) and infrared filter (780 nm long pass; Midopt, BN810-43), positioned approximately 8 inches from the mouse. An off-axis infrared light source (two infrared LEDs; 850 nm, Digikey; adjustable in intensity and position) was used to yield a high-quality image of the surface of the eye and a dark pupil. Images (504×500 pixels)

were collected at 15 Hz during the imaging experiment, and at 143 Hz for all other experiments, using a National Instruments PCIe-8233 GigE vision frame grabber. To achieve a wide dynamic range of pupil fluctuations, an additional near-ultraviolet LED was positioned above the animal and provided low intensity illumination that was adjusted such that the animal's pupil was approximately mid-range in diameter following placement of the animal in the set-up, and did not saturate the eye when the animal walked. Near-ultraviolet LED light levels were lower during two-photon imaging experiments, to avoid noise on the photo-multiplier tubes. We continuously measured treadmill motion using a rotary optical encoder (Accu, SL# 2204490) with a resolution of 8,000 counts/revolution.

Acquisition of cholinergic axon data (in vivo calcium imaging)

The methodology for in vivo GCaMP imaging of cholinergic axons is the same as we used previously, except that we used the Ai162 reporter line (Reimer et. al 2016). In brief, two-photon imaging was performed from right auditory cortex with a fast resonant scanning system (ThorLabs rotating Bergamo). The imaging frame rate was 15 Hz. Excitation was via a Ti–sapphire laser (Insight DS+, Spectra Physics) tuned to 930 nm, with either a 16 × (0.8 NA, Nikon) or 25 × (1.1 NA, Nikon) objective at a depth of 100-200 um from pial surface. Power out of the objective was controlled by calibrated rotations of a half-wave attenuator and depended on the magnification of the scan but was typically 30–40 mW. We used Scan Image (Vidrio) to control the imaging system.

Analysis of leak fraction and filtering

We characterized the extent of current leakage and filtering (Fig. S1) as follows. First, leak fraction was defined as:

$$L = 1 - \frac{A_m}{A_i} \qquad \text{Eq. 1}$$

where L was the session-wise leak fraction, A_m was the mean across the minimum measured amplitude for each unique pulse widths and rate (to avoid filtering effects [see below], we excluded the 0.1 and 0.2 ms pulse widths), and A_i was the session-wise minimum intended amplitude (0.1 mA in the ungrounded sessions; 0.1, 0.2, 0.4 or 0.6 mA in the grounded sessions). Second, the extent of filtering was modeled with the following sigmoidal function:

$$A_m = \frac{s}{1+\exp{(-a(W-b))}} \qquad \text{Eq. 2}$$

where A_m was a vector of the mean measured amplitudes for each pulse width, W was a vector of the unique pulse widths (0.1, 0.2, 0.4 and 0.8 ms), and s, a and b were the free parameters of the fit.

Analysis of pupil and eyelid data

All analyses were performed using custom-made Python scripts, unless stated otherwise.

Preprocessing. We measured pupil size and exposed eye area from the videos of the animal's eye using DeepLabCut (Mathis et al., 2018). In approximately 1000 training frames randomly sampled across all sessions, we manually identified 8 points spaced at approximately evenly around the pupil, and 8 points evenly spaced around the eyelids. The network (resnet 110) was trained with default parameters. In order

16

to increase the network's speed and accuracy when labeling (unseen) frames of all videos, we specified video-wise cropping values in the DeepLabCut configuration file that corresponded to a square around the eye. The pupil size (exposed eye area) was computed as the area of an ellipse fitted to the detected pupil (exposed eye) points. If two or more point were labeled with a likelihood smaller than 0.1 (e.g., during blinks), we did not fit an ellipse, but flagged the frame as missing data. We then applied to the pupil (exposed eye) time series of each measurement session: (i) resampling to 50 Hz, (ii) linear interpolation of missing or poor data due to blinks (interpolation time window, from 150 ms before until 150 ms after missing data; blinks were detected by a custom algorithm that marked outliers in the z-scored temporal derivative of the pupil time series), (iii) low-pass filtering (third-order Butterworth, cut-off: 3 Hz), and (iv) conversion to percentage of the 99.9 percentile of the time series.

Quantification of VNS-evoked responses. We quantified VNS-evoked pupil (or exposed eye) responses as the mean pupil size (exposed eye area) from 2.5 s to 7.5 s after VNS onset (colored bars in Fig. 2A), with the mean pre-trial baseline pupil size (exposed eye area) in the 5 s before VNS subtracted out. The background luminance during the calcium imaging was lower than for the other experiments (Fig. S5D), and we observed substantially longer lasting pupil responses. Therefore, for the calcium imaging sessions, we quantified VNS-evoked pupil responses as the mean pupil size from 10 s to 30 s after VNS onset (colored bars in Fig. S5D), with the mean pre-trial baseline pupil (exposed eye) size in the 20 s before VNS subtracted out. We corrected VNS-evoked pupil (exposed eye) responses for a general (not related to VNS) reversion towards the mean (illustrated in Fig. 4A,B). To do so, we (i) computed 'pseudo' baseline and response measures in the 60 seconds prior to each VNS that had the same durations and relative delays as specified above, (ii) fitted the relationship between these pseudo baseline and response measures with a cubic function, (iii) predicted response measures (reflecting the predicted reversion to the mean) based on the observed pre-VNS baseline measures, and (iv) subtracted those values from the observed VNS-evoked responses measures.

Analysis of walking data

The instantaneous velocity data was resampled to 50 Hz. We quantified VNS-evoked walking speed as the mean speed in the 10 s after VNS onset. We defined VNS-evoked walking probability as the fraction of pulses for which the absolute walking speed exceeded 0.05 cm/s (Fig. S6 and S7A). We corrected for reversion to the mean in the same way as done for the VNS-evoked pupil responses (see above).

Analysis of calcium imaging data

Preprocessing. All frames in the image stack were co-registered using a custom two-step approach that we contributed to the Suite2p master repository on Github (Pachitariu et al., 2017). This involved (i) running Suite2p's default rigid registration step and computing a new reference image as the mean across the co-registered frames, and (ii) rerunning Suite2p's rigid registration using this new (enhanced) reference. We defined one region of interest per session as follows. First, for each pixel we computed VNS-evoked calcium responses as the mean fluorescence from 2.5 s to 7.5 s after VNS onset (colored bars in Fig. 5C), with the mean pre-trial baseline fluorescence in the 5 s before VNS subtracted out. Second, we tested all calcium response measures against 0 (irrespective of VNS parameters; Fig. 5A), using a cluster-based one sample t-test that corrected for multiple comparisons. Third, we defined the region of interest as all pixels whose time series exhibited significant VNS-evoked calcium responses (p < 0.01; cluster-corrected). Per session, we then averaged the fluorescence time series of pixels within the region of interest, and applied:

17

(i) resampling to 50 Hz, (ii) low-pass filtering (third-order Butterworth, cut-off: 3 Hz), (iii) linear de-trending of bleach-related rundown in the calcium signals, and (iv) rescaled to percentage of the 99.9 percentile of the time series values.

Quantification of VNS-evoked responses. We quantified VNS-evoked calcium responses as the mean fluorescence from 2.5 s to 7.5 s after VNS onset (colored bars in Fig. 2A), with the pre-trial baseline fluorescence in the 5 s before VNS subtracted out. We corrected for reversion to the mean in the same way as done for the VNS-evoked pupil responses (see above).

Analysis of parametric VNS dependence

Log-logistic function. The relationship between VNS parameters (amplitude, width and rate) and VNS-evoked responses (pupil, calcium, walking, exposed eye) was modeled with the following log-logistic function:

$$P = \frac{s}{1+(A/a_1)^{-b_1}} \times \frac{1}{1+(W/a_2)^{-b_2}} \times \frac{1}{1+(R/a_3)^{-b_3}} \qquad \text{Eq. 3}$$

where P was a vector of the VNS-evoked pupil (or calcium, walking, exposed eye) responses, A was a vector the pulse amplitudes, W was a vector of the pulse widths, R was a vector of the pulse rates, and s, a_1, a_2, a_3, b_1, b_2, b_3 were the free parameters of the fit. Likewise, the relationship between VNS parameters (charge/pulse and rate) and VNS-evoked responses (pupil, calcium, walking, exposed eye) was modeled with:

$$P = \frac{s}{1+(C/a_1)^{-b_1}} \times \frac{1}{1+(R/a_2)^{-b_2}} \qquad \text{Eq. 4}$$

where C was a vector the pulse charges (amplitude $\times$ width).

Mediation analysis. We performed a mediation analysis to characterize the interaction between VNS parameters, VNS-evoked pupil responses and VNS-evoked calcium responses (Figs. 7 & S7). We fitted the following linear regression models based on standard mediation path analysis:

$$P = i_0 1 + cN \qquad \text{Eq. 5}$$

$$C = i_1 1 + aN \qquad \text{Eq. 6}$$

$$P = i_2 1 + c'P + bC \qquad \text{Eq. 7}$$

where P was a vector of VNS-evoked pupil responses, C was a vector of the VNS-evoked calcium responses, N was a vector of the predicted VNS-evoked nerve engagement due (see below), and c, c', a, b, i_0, i_1 and i_2 were the free parameters of the fit. The parameters were fit using freely available R-software (Rosseel, 2012).

We constructed vector N of the predicted VNS-evoked nerve engagement in a way that met two objectives: (i) reducing the three-dimensional VNS parameter space (amplitude $\times$ width $\times$ rate) to a one-dimensional independent variable, and (ii) allowing all interactions to be modeled with linear regressions

18

(instead of the log-logistic function). We constructed vector *N* with a 20-fold cross-validation procedure. In every iteration, 95% of data was used to fit the relationship between VNS parameters (amplitude, width and rate) and VNS-evoked pupil responses with the log-logistic function described above; the remaining 5% of data as used to predict VNS-evoked nerve engagement by plugging the corresponding pulse amplitudes, widths and rates in the fitted function.

Statistical comparisons

We used the one-sample t-test to test for significant differences between VNS-evoked pupil, walking or exposed eye responses and 0 (Figs. 3, 6, S2, S3 & S5). We refrained from testing the VNS-evoked calcium responses against 0, which would be 'double dipping' because of the way we defined our region of interest (see *Analysis of calcium imaging data*). Instead, we used the paired-sample t-test to test for significant differences between VNS-evoked calcium responses in the highest four charge bins and those responses in the lowest charge bin (Figs. 5 & 7). Thus, this test does not quantify the effect of VNS on evoked calcium responses per se, but addresses the orthogonal question of the *parameter dependence* of VNS-evoked calcium responses. In all cases, we corrected for multiple comparisons with false discovery rate (FDR).

We used sequential polynomial regression analysis(Draper and Smith, 1998) to systematically characterize the relationship between VNS-evoked pupil responses and pre-VNS pupil baseline size (Fig. 4):

$$P = \beta_0 1 + \beta_1 B + \beta_2 B^2 + \beta_3 B^3 \qquad \text{Eq. 8}$$

where *P* was a vector of VNS-evoked pupil responses, *B* was a vector of pre-VNS baseline pupil size measures, and *β* as polynomial coefficients. The corresponding regressors were orthogonalized, and each model was sequentially tested in a serial hierarchical analysis, based on *F*-statistics. The analysis tested whether adding the next higher order model yielded a significantly better description of the response than the respective lower order model. We tested models from the zeroth order up to the third order.

We used the non-parametric cluster-level paired t-test within the MNE implementation(Gramfort et al., 2014; Maris and Oostenveld, 2007) to test VNS-evoked calcium responses against 0 (10K permutations; cluster-correction threshold, $p < 0.01$; Fig. 5A).

Data and code sharing

The data are publicly available on [to be filled in upon publication]. Analysis scripts are publicly available on [to be filled in upon publication].

19

REFERENCES

Aston-Jones, G., and Cohen, J.D. (2005). An integrative theory of locus coeruleus-norepinephrine function: adaptive gain and optimal performance. Annu Rev Neurosci *28*, 403-450.

Bailey, P., and Bremer, F. (1938). A sensory cortical representation of the vagus nerve: with a note on the effects of low blood pressure on the cortical electrogram. Journal of Neurophysiology *1*, 405-412.

Ballinger, E.C., Ananth, M., Talmage, D.A., and Role, L.W. (2016). Basal forebrain cholinergic circuits and signaling in cognition and cognitive decline. Neuron *91*, 1199-1218.

Breton-Provencher, V., and Sur, M. (2019). Active control of arousal by a locus coeruleus GABAergic circuit. Nature neuroscience *22*, 218.

Chae, J.-H., Nahas, Z., Lomarev, M., Denslow, S., Lorberbaum, J.P., Bohning, D.E., and George, M.S. (2003). A review of functional neuroimaging studies of vagus nerve stimulation (VNS). Journal of psychiatric research *37*, 443-455.

Colizoli, O., De Gee, J.W., Urai, A.E., and Donner, T.H. (2018). Task-evoked pupil responses reflect internal belief states. Scientific reports *8*, 13702.

Dayan, P. (2012). Twenty-five lessons from computational neuromodulation. Neuron *76*, 240-256.

de Gee, J.W., Colizoli, O., Kloosterman, N.A., Knapen, T., Nieuwenhuis, S., and Donner, T.H. (2017). Dynamic modulation of decision biases by brainstem arousal systems. Elife *6*, e23232.

de Gee, J.W., Knapen, T., and Donner, T.H. (2014). Decision-related pupil dilation reflects upcoming choice and individual bias. Proceedings of the National Academy of Sciences *111*, E618-E625.

De Ridder, D., Vanneste, S., Engineer, N.D., and Kilgard, M.P. (2014). Safety and efficacy of vagus nerve stimulation paired with tones for the treatment of tinnitus: a case series. Neuromodulation: Technology at the Neural Interface *17*, 170-179.

Draper, N.R., and Smith, H. (1998). Applied regression analysis, Vol 326 (John Wiley & Sons).

Edwards, C.A., Kouzani, A., Lee, K.H., and Ross, E.K. (2017). Neurostimulation devices for the treatment of neurologic disorders. Paper presented at: Mayo Clinic Proceedings (Elsevier).

Ellrich, J. (2011). Transcutaneous vagus nerve stimulation. Eur Neurol Rev *6*, 254-256.

Engineer, C.T., Hays, S.A., and Kilgard, M.P. (2017). Vagus nerve stimulation as a potential adjuvant to behavioral therapy for autism and other neurodevelopmental disorders. Journal of neurodevelopmental disorders *9*, 20.

Engineer, N.D., Riley, J.R., Seale, J.D., Vrana, W.A., Shetake, J.A., Sudanagunta, S.P., Borland, M.S., and Kilgard, M.P. (2011). Reversing pathological neural activity using targeted plasticity. Nature *470*, 101.

Evans, M., Verma-Ahuja, S., Naritoku, D., and Espinosa, J. (2004). Intraoperative human vagus nerve compound action potentials. Acta neurologica scandinavica *110*, 232-238.

Fang, J., Rong, P., Hong, Y., Fan, Y., Liu, J., Wang, H., Zhang, G., Chen, X., Shi, S., and Wang, L. (2016). Transcutaneous vagus nerve stimulation modulates default mode network in major depressive disorder. Biological psychiatry *79*, 266-273.

George, M.S., and Aston-Jones, G. (2010). Noninvasive techniques for probing neurocircuitry and treating illness: vagus nerve stimulation (VNS), transcranial magnetic stimulation (TMS) and transcranial direct current stimulation (tDCS). Neuropsychopharmacology *35*, 301.

George, M.S., Sackeim, H.A., Rush, A.J., Marangell, L.B., Nahas, Z., Husain, M.M., Lisanby, S., Burt, T., Goldman, J., and Ballenger, J.C. (2000). Vagus nerve stimulation: a new tool for brain research and therapy∗. Biological psychiatry *47*, 287-295.

George, M.S., Ward Jr, H.E., Ninan, P.T., Pollack, M., Nahas, Z., Anderson, B., Kose, S., Howland, R.H., Goodman, W.K., and Ballenger, J.C. (2008). A pilot study of vagus nerve stimulation (VNS) for treatment-resistant anxiety disorders. Brain stimulation *1*, 112-121.

Gilzenrat, M.S., Nieuwenhuis, S., Jepma, M., and Cohen, J.D. (2010). Pupil diameter tracks changes in control state predicted by the adaptive gain theory of locus coeruleus function. Cognitive, Affective, & Behavioral Neuroscience *10*, 252-269.

Götz, J., Bodea, L.-G., and Goedert, M. (2018). Rodent models for Alzheimer disease. Nature Reviews Neuroscience *19*, 583-598.

Gramfort, A., Luessi, M., Larson, E., Engemann, D.A., Strohmeier, D., Brodbeck, C., Parkkonen, L., and Hämäläinen, M.S. (2014). MNE software for processing MEG and EEG data. Neuroimage *86*, 446-460.

Groves, D.A., Bowman, E.M., and Brown, V.J. (2005). Recordings from the rat locus coeruleus during acute vagal nerve stimulation in the anaesthetised rat. Neuroscience letters *379*, 174-179.

Groves, D.A., and Brown, V.J. (2005). Vagal nerve stimulation: a review of its applications and potential mechanisms that mediate its clinical effects. Neuroscience & Biobehavioral Reviews *29*, 493-500.

Hulsey, D.R., Hays, S.A., Khodaparast, N., Ruiz, A., Das, P., Rennaker II, R.L., and Kilgard, M.P. (2016). Reorganization of motor cortex by vagus nerve stimulation requires cholinergic innervation. Brain stimulation *9*, 174-181.

Hulsey, D.R., Riley, J.R., Loerwald, K.W., Rennaker II, R.L., Kilgard, M.P., and Hays, S.A. (2017). Parametric characterization of neural activity in the locus coeruleus in response to vagus nerve stimulation. Experimental neurology *289*, 21-30.

Joshi, S., Li, Y., Kalwani, R.M., and Gold, J.I. (2016). Relationships between pupil diameter and neuronal activity in the locus coeruleus, colliculi, and cingulate cortex. Neuron *89*, 221-234.

Keute, M., Demirezen, M., Graf, A., Mueller, N.G., and Zaehle, T. (2019). No modulation of pupil size and event-related pupil response by transcutaneous auricular vagus nerve stimulation (taVNS). Scientific reports *9*, 1-10.

Kilgard, M.P., and Merzenich, M.M. (1998). Cortical map reorganization enabled by nucleus basalis activity. Science *279*, 1714-1718.

Krahl, S.E., Clark, K.B., Smith, D.C., and Browning, R.A. (1998). Locus coeruleus lesions suppress the seizure-attenuating effects of vagus nerve stimulation. Epilepsia *39*, 709-714.

Kret, M.E., and Sjak-Shie, E.E. (2019). Preprocessing pupil size data: Guidelines and code. Behavior research methods *51*, 1336-1342.

Larsen, R.S., and Waters, J. (2018). Neuromodulatory correlates of pupil dilation. Frontiers in neural circuits *12*, 21.

Maris, E., and Oostenveld, R. (2007). Nonparametric statistical testing of EEG-and MEG-data. Journal of neuroscience methods *164*, 177-190.

Mathis, A., Mamidanna, P., Cury, K.M., Abe, T., Murthy, V.N., Mathis, M.W., and Bethge, M. (2018). DeepLabCut: markerless pose estimation of user-defined body parts with deep learning (Nature Publishing Group).

McGinley, M.J., David, S.V., and McCormick, D.A. (2015a). Cortical membrane potential signature of optimal states for sensory signal detection. Neuron *87*, 179-192.

McGinley, M.J., Vinck, M., Reimer, J., Batista-Brito, R., Zagha, E., Cadwell, C.R., Tolias, A.S., Cardin, J.A., and McCormick, D.A. (2015b). Waking state: rapid variations modulate neural and behavioral responses. Neuron *87*, 1143-1161.

Murphy, P.R., O'Connell, R.G., O'Sullivan, M., Robertson, I.H., and Balsters, J.H. (2014). Pupil diameter covaries with BOLD activity in human locus coeruleus. Human brain mapping *35*, 4140-4154.

Nahas, Z., Marangell, L.B., Husain, M.M., Rush, A.J., Sackeim, H.A., Lisanby, S.H., Martinez, J.M., and George, M.S. (2005). Two-year outcome of vagus nerve stimulation (VNS) for treatment of major depressive episodes. The Journal of clinical psychiatry.

Naritoku, D.K., Terry, W.J., and Helfert, R.H. (1995). Regional induction of fos immunoreactivity in the brain by anticonvulsant stimulation of the vagus nerve. Epilepsy research *22*, 53-62.

Nichols, J., Nichols, A., Smirnakis, S., Engineer, N., Kilgard, M., and Atzori, M. (2011). Vagus nerve stimulation modulates cortical synchrony and excitability through the activation of muscarinic receptors. Neuroscience *189*, 207-214.

Pachitariu, M., Stringer, C., Dipoppa, M., Schröder, S., Rossi, L.F., Dalgleish, H., Carandini, M., and Harris, K.D. (2017). Suite2p: beyond 10,000 neurons with standard two-photon microscopy. Biorxiv, 061507.

Parikh, V., Kozak, R., Martinez, V., and Sarter, M. (2007). Prefrontal acetylcholine release controls cue detection on multiple timescales. Neuron *56*, 141-154.

Qing, K.Y., Wasilczuk, K.M., Ward, M.P., Phillips, E.H., Vlachos, P.P., Goergen, C.J., and Irazoqui, P.P. (2018). B fibers are the best predictors of cardiac activity during Vagus nerve stimulation. Bioelectronic Medicine *4*, 5.

Reimer, J., Froudarakis, E., Cadwell, C.R., Yatsenko, D., Denfield, G.H., and Tolias, A.S. (2014). Pupil fluctuations track fast switching of cortical states during quiet wakefulness. Neuron *84*, 355-362.

Reimer, J., McGinley, M.J., Liu, Y., Rodenkirch, C., Wang, Q., McCormick, D.A., and Tolias, A.S. (2016). Pupil fluctuations track rapid changes in adrenergic and cholinergic activity in cortex. Nature communications *7*, 13289.

Rosseel, Y. (2012). An R package for structural equation modeling and more. version 0.5-12 (BETA).

Rush, A.J., Marangell, L.B., Sackeim, H.A., George, M.S., Brannan, S.K., Davis, S.M., Howland, R., Kling, M.A., Rittberg, B.R., and Burke, W.J. (2005). Vagus nerve stimulation for treatment-resistant depression: a randomized, controlled acute phase trial. Biological psychiatry *58*, 347-354.

Schriver, B.J., Bagdasarov, S., and Wang, Q. (2018). Pupil-linked arousal modulates behavior in rats performing a whisker deflection direction discrimination task. Journal of neurophysiology *120*, 1655-1670.

Sjögren, M.J., Hellström, P.T., Jonsson, M.A., Runnerstam, M., Silander, H.C., and Ben-Menachem, E. (2002). Cognition-enhancing effect of vagus nerve stimulation in patients with Alzheimer's disease: A pilot study. The Journal of clinical psychiatry.

Varazzani, C., San-Galli, A., Gilardeau, S., and Bouret, S. (2015). Noradrenaline and dopamine neurons in the reward/effort trade-off: a direct electrophysiological comparison in behaving monkeys. Journal of Neuroscience *35*, 7866-7877.

Vinck, M., Batista-Brito, R., Knoblich, U., and Cardin, J.A. (2015). Arousal and locomotion make distinct contributions to cortical activity patterns and visual encoding. Neuron *86*, 740-754.

Ward, M.P., Qing, K.Y., Otto, K.J., Worth, R.M., John, S.W., and Irazoqui, P.P. (2014). A flexible platform for biofeedback-driven control and personalization of electrical nerve stimulation therapy. IEEE Transactions on Neural Systems and Rehabilitation Engineering *23*, 475-484.

Warren, C.M., Tona, K.D., Ouwerkerk, L., Van Paridon, J., Poletiek, F., van Steenbergen, H., Bosch, J.A., and Nieuwenhuis, S. (2019). The neuromodulatory and hormonal effects of transcutaneous vagus nerve stimulation as evidenced by salivary alpha amylase, salivary cortisol, pupil diameter, and the P3 event-related potential. Brain stimulation *12*, 635-642.

Waschke, L., Tune, S., and Obleser, J. (2019). Neural desynchronization and arousal differentially shape brain states for optimal sensory performance. bioRxiv, 582353.

Zabara, J. (1985). Peripheral control of hypersynchonous discharge in epilepsy. Electroencephalogr Clin Neurophysiol *61*, S162.
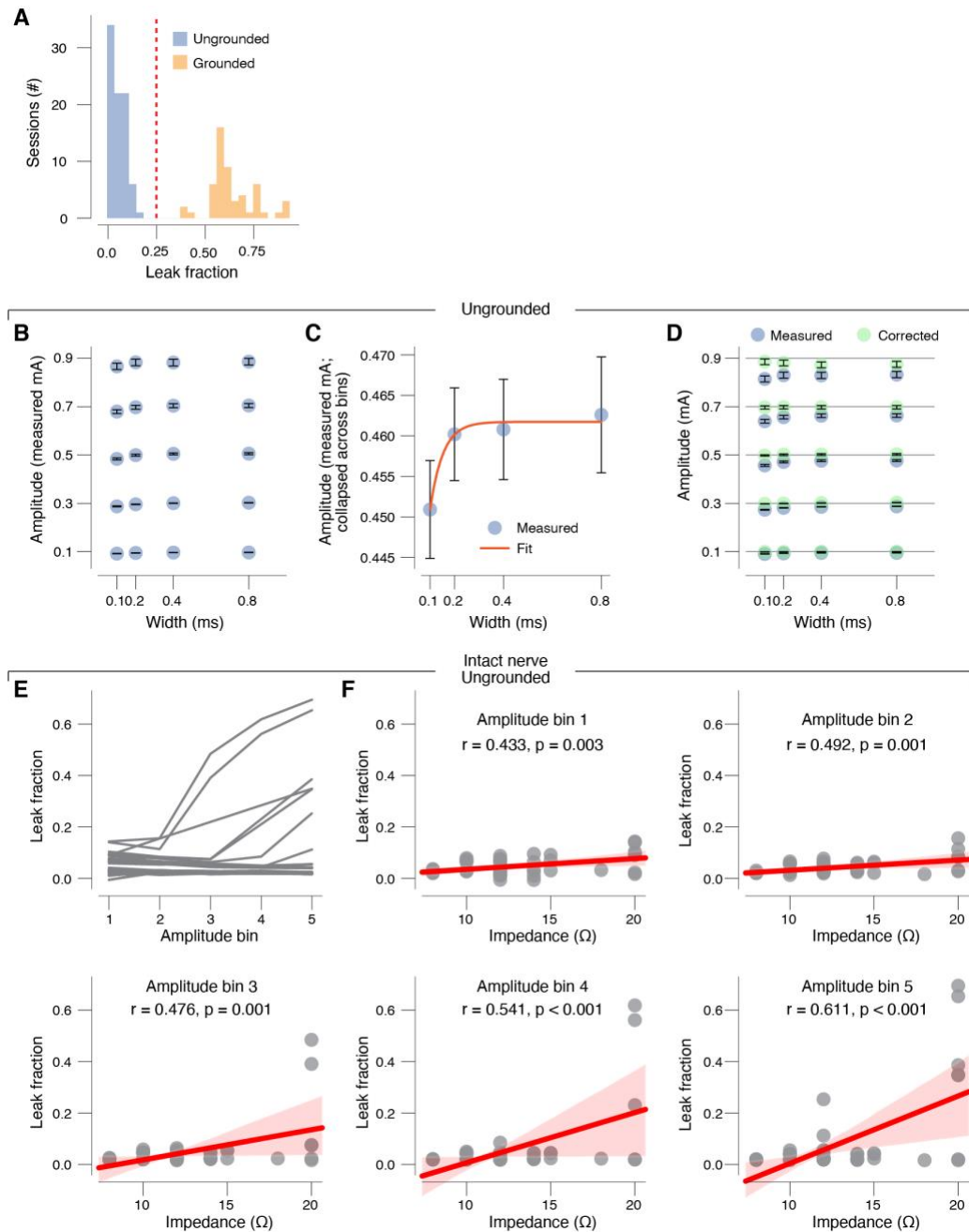
SUPPLEMENTARY FIGURES

Figure S1. (A) Histogram of session-wise observed leak fraction (extent of current loss for the smallest amplitude pulses with the largest two pulse widths; see Materials and Methods). **(B)** Measured pulse amplitudes for five amplitude and four width bins, averaged across train rates. Error bars, s.e.m. across sessions. All sessions in ungrounded conditions are included (intact, single cut, and double cut nerve). **(C)** Same as in B, but collapsed across amplitude bins. Red line, fitted sigmoid (see Materials and Methods). **(D)** Same as in B, but including amplitude measures that were corrected for leak and filtering (green symbols). Black horizontal lines indicate total applied current. **(E)** Observed leak fraction for each amplitude bin (averaged across highest two pulse widths and all train rates). Eech line is a session. **(F)** Relationship between observed leak fraction and measured cuff electrode impedance.

Each panel is for the indicated pulse amplitude bin. Each data point is a session; red lines are fitted 1_{st} order polynomial; stats are Pearson correlation.
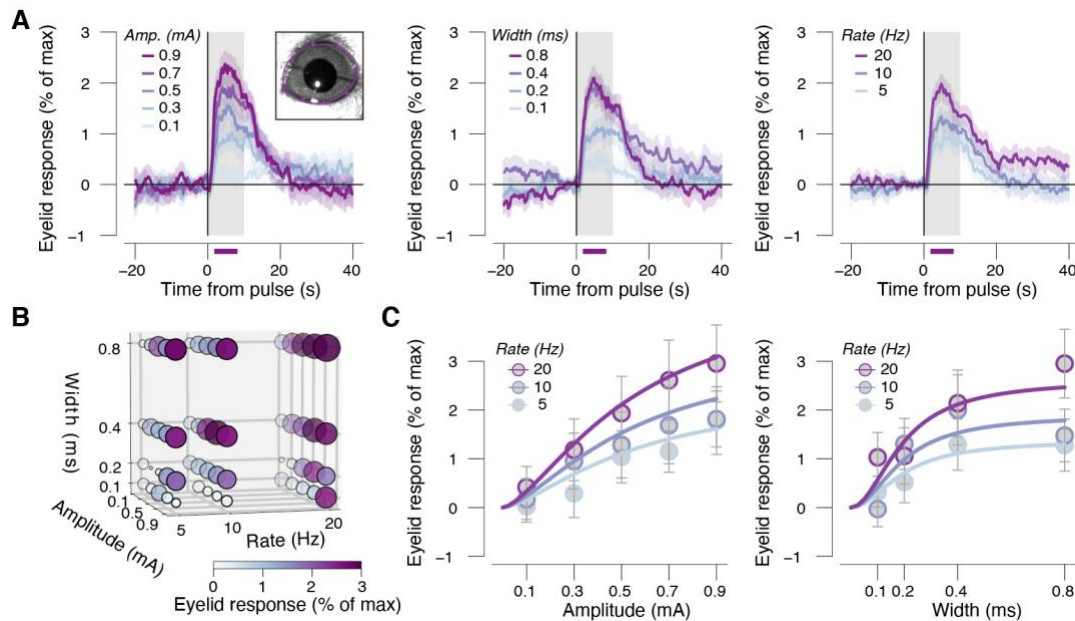
Figure S2. (A) VNS-evoked exposed eye area response time-courses separately for each pulse amplitude (left), width (middle) and rate (right), collapsed across two other stimulation parameters. Grey window, 10 second VNS train; red bars, interval for VNS-evoked exposed eye area scalar measures (see Materials and Methods); shading, s.e.m. **(B)** VNS-evoked exposed eye area scalar measure for all 60 unique parameter combinations. Response magnitude is indicated by circle size and color. **(C)** VNS-evoked exposed eye area scalars plotted separately for pulse amplitudes and rates (binned across width, left) and separately for pulse widths and rates (binned across amplitude, right). Colored lines, fitted log-logistic functions (Materials and Methods); error bars, s.e.m. × 1.96 (95% confidence interval of the mean).

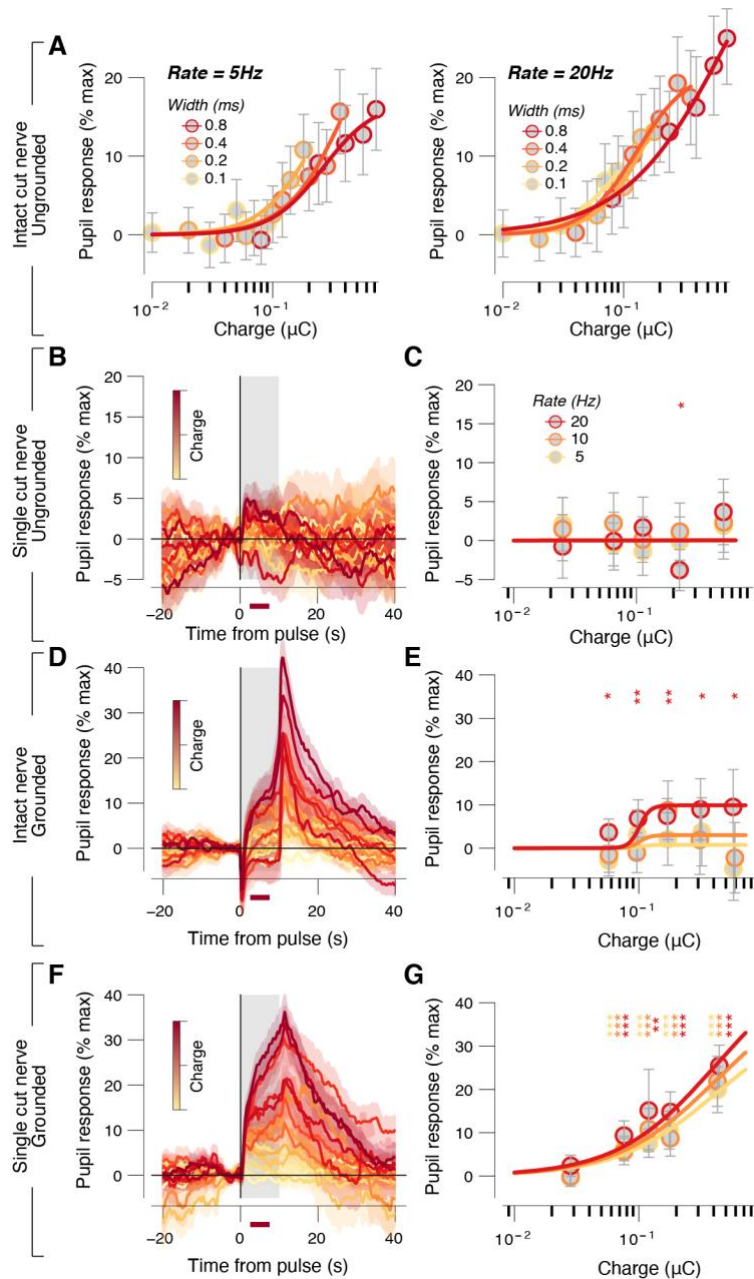**Figure S3. (A)** VNS-evoked pupil response measures separately per pulse charge (amplitude × width) and width for 5 Hz (left) and 20 Hz (right) trains. Colored lines, fitted log logistic function (see Materials and Methods); error bars, s.e.m. × 1.96 (95% confidence interval of the mean). **(B)** VNS-evoked pupil time-courses in the single cut ungrounded sessions. Each trace is a charge/pulse bin and train rate. Grey window, VNS train; red bar, interval for VNS-evoked pupil response scalar measures (see Materials and Methods); shading, s.e.m. **(C)** VNS-evoked pupil response measures, in the single cut ungrounded sessions, separately per charge/pulse bin and train rate. Colored lines, fitted log logistic function (see Materials and Methods); stats, one sample t-test (tested against 0; ***p < 0.001, **p < 0.01; *p < 0.05, corrected for false discovery rate); error bars, s.e.m. × 1.96 (95% confidence interval of the mean). **(D-E)** Same as in B-C, but for intact nerve grounded sessions. **(F-G)** Same as in B-C, but for the single cut nerve grounded sessions.
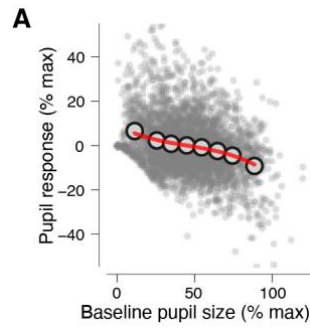
Figure S4. Scatter-plot of relationship between pseudo-VNS pupil responses and pseudo-baseline pupil size (panel A, left). Each small data point is an individual VNS pseudo-train; large data points are the data binned by pseudo baseline pupil size (8 bins); red line, same fitted cubic function as in main Figure 4B (Materials and Methods).
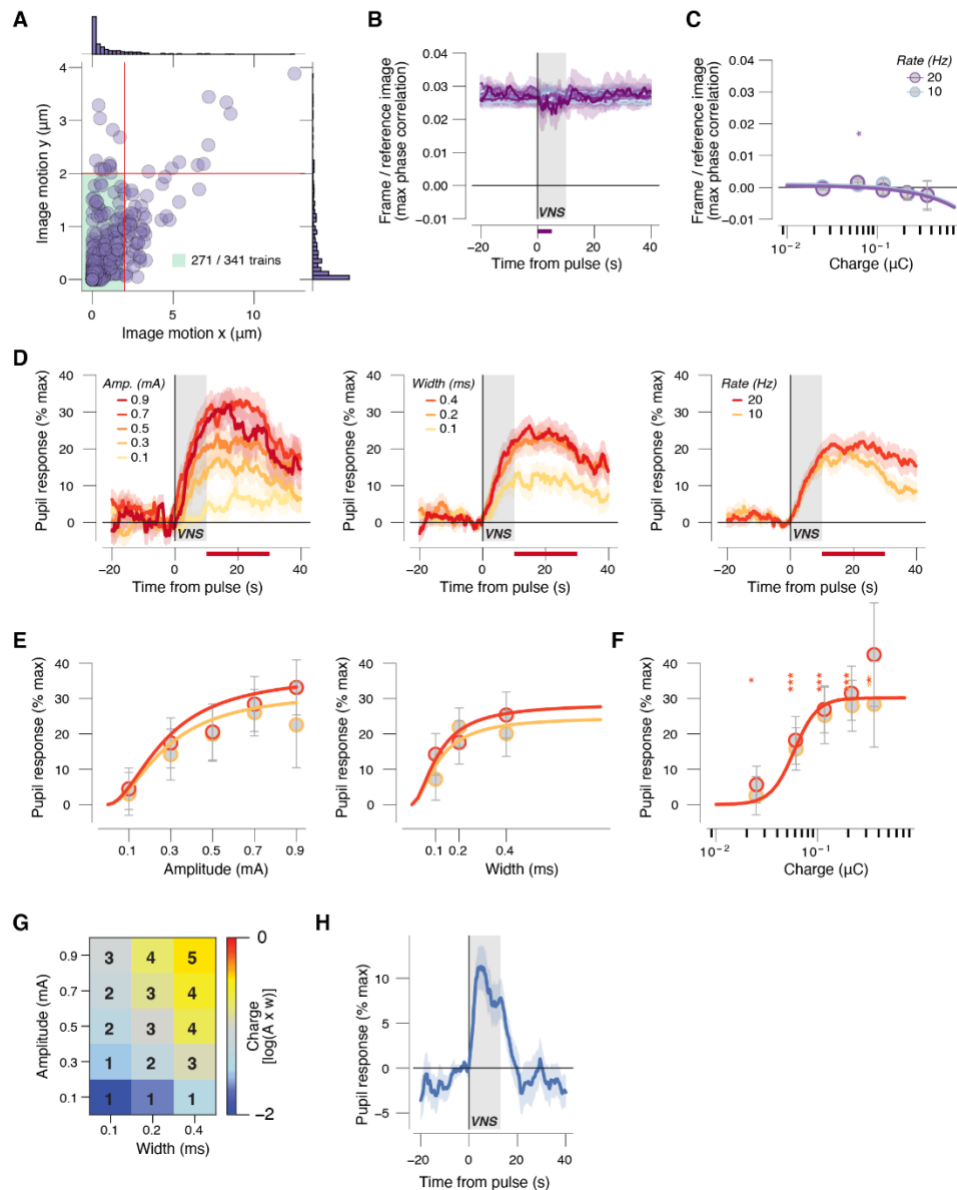
Figure S5. (A) Scatter plot of estimated image motion (from Suite2p's rigid registration step; Materials and Methods) in x and y. Data points, VNS pulses; green window, analysis inclusion zone (Materials and Methods). **(B)** Correspondence between co-registered frame and the reference image time-locked to VNS separately for pulse charge and collapsed across pulse rate. Grey window, VNS train; purple bar, interval for VNS-evoked correspondence measures (Materials and Methods); shading, s.e.m. **(C)** VNS-evoked correspondence measures separately per pulse charge bin and pulse rate. Colored lines, fitted log logistic function (Materials and Methods); stats, one sample t-test (tested against 0; ***p < 0.001, **p < 0.01; *p < 0.05 false discovery rate corrected); error bars, s.e.m. × 1.96 (95% confidence interval of the mean). **(D)** VNS-evoked pupil responses separately for pulse amplitudes (left), widths (middle) and rates (right) collapsed across two other stimulation parameters. Grey window, VNS pulse (10 s); purple bars, interval for VNS-evoked pupil response measures (Materials and Methods); shading, s.e.m. **(E)** VNS-evoked pupil response measures separately for pulse amplitudes and rates (left) and separately for pulse widths and rates (right). Colored lines, fitted log logistic function (Materials and Methods); error bars, s.e.m. × 1.96 (95% confidence interval of the mean). **(F)** As C, but for VNS-evoked pupil responses. **(G)** Grid indicating the five equal size charge bins used to reduce the parameter space in imaging experiments. **(H)** VNS-evoked pupil responses in pupil luminance control experiment (Materials and Methods).
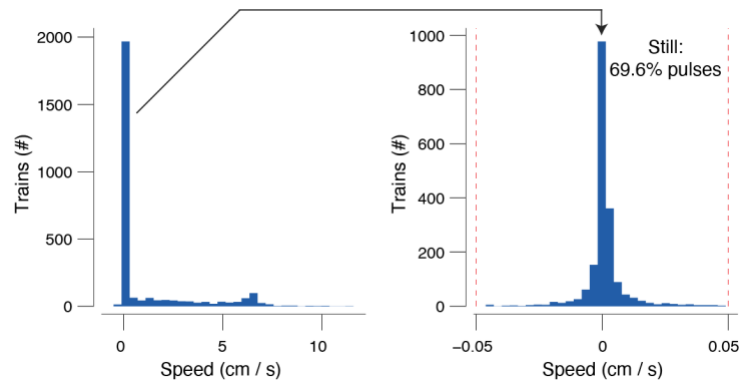
28

Figure S6. Left: histogram of VNS-evoked walking speed. Right: as left, but zoomed in on the large peak around zero walking speed. Dashed red line, cutoff for defining walking.
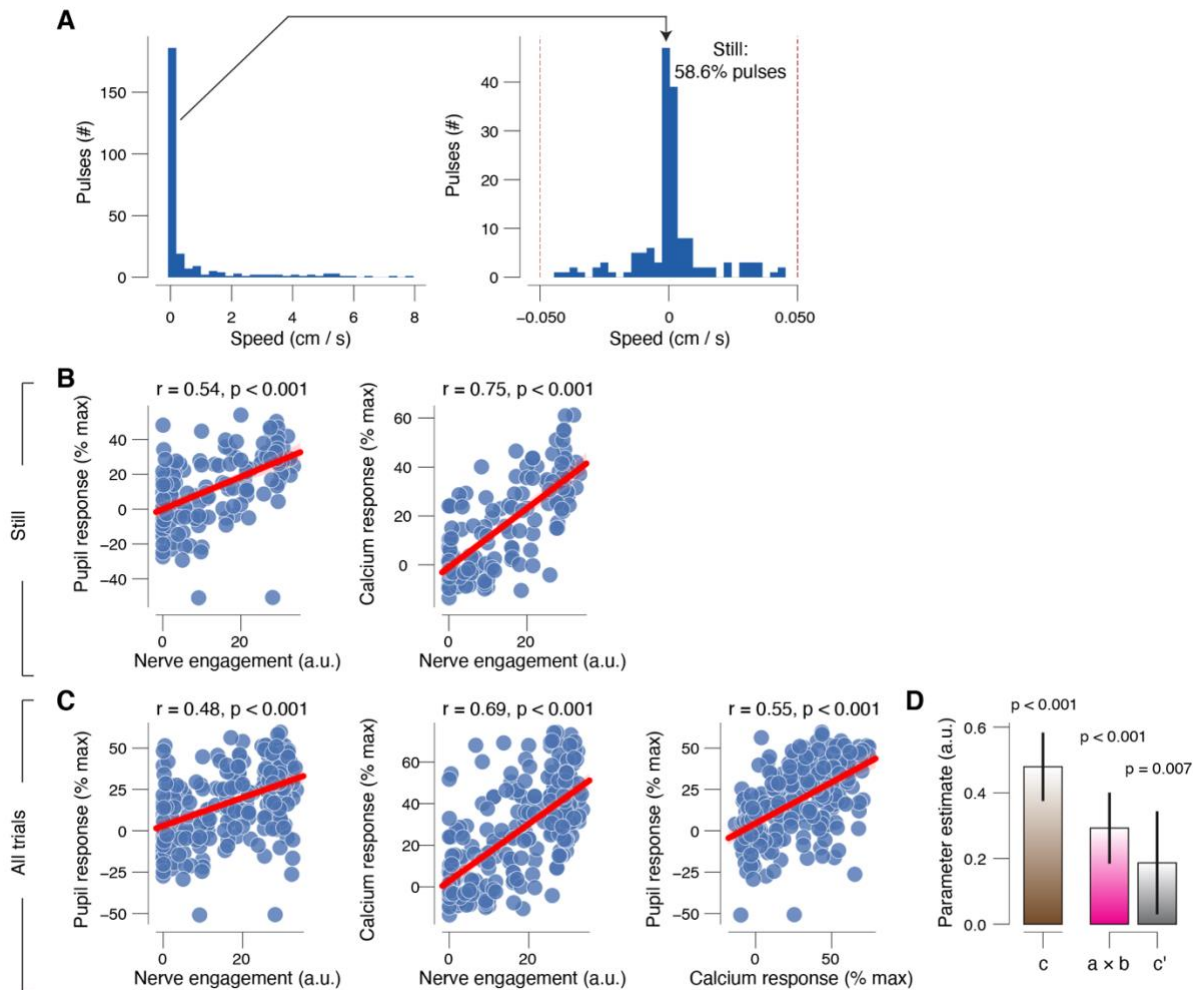
Figure S7. (A) Left: histogram of VNS-evoked walking speed. Right: as left, but zoomed in on the large peak. Dashed red line, cutoff for defining walking. **(B)** Relationship between VNS-evoked pupil responses (left) or calcium responses (right) and VNS in absence of walking. Data points, individual VNS pulses; red line, fitted 1_{st} order polynomial, stats, Pearson correlation. **(C)** As B, but for all trials, irrespective of walking. **(D)** For all trials, irrespective of walking: fitted regression coefficients of the total effect (brown), indirect path (mediation; pink) and the direct path (grey). Error bars, 95% confidence interval (bootstrapped; 5000K); stats, fraction of bootstrapped coefficients smaller than 0.